

pubs.acs.org/JPCC Article

# Electrochemical Structure of the Plasma-Liquid Interface

Trey Oldham and Elijah Thimsen\*



Cite This: J. Phys. Chem. C 2022, 126, 1222-1229



**ACCESS** I

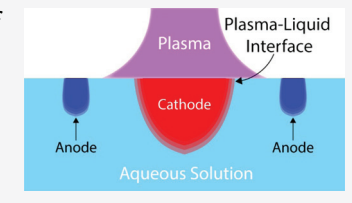


Metrics & More





ABSTRACT: Nonthermal atmospheric pressure plasma in contact with a liquid yields a variety of energetic photons, ions, and electrons, which can be transported into the plasma-liquid interface (PLI). Similar to the electrochemical interface formed between a solid electrode and electrolyte in conventional electrochemical systems, the charge-transfer process across the PLI is able to promote reduction-oxidation (redox) reactions. However, in the case of free plasma jets in contact with liquids, the absence of solid electrodes obscures the spatial locations of the electrochemical half-reactions. Herein, we present a spatial electrochemical measurement



technique used to characterize an aqueous solution in contact with an atmospheric pressure plasma jet. The technique is based on measuring the potential difference between two identical Ag/AgCl electrochemical electrodes positioned at different locations within the solution. More specifically, electrochemical maps were made by measuring the potential of one electrochemical electrode positioned at different locations near the PLI with respect to the other electrochemical electrode positioned far away from the PLI in the bulk solution. Regions in the map with negative and positive potential differences between these electrochemical electrodes were used to identify the electrodeless cathode and anode, respectively. Visualization of the spatial distribution of molecular colorimetric redox indicators by multispectral imaging revealed that reduction was occurring near the plasma jet centerline while oxidation was occurring further away in solution, which constitutes an independent confirmation of the electrochemical maps.

# **■ INTRODUCTION**

Interactions between atmospheric pressure plasma and liquid media have attracted attention owing to their great potential in the fields of medicine, <sup>1-3</sup> nanomaterial synthesis, <sup>4-6</sup> and wastewater treatment. <sup>7-9</sup> These applications utilize nonthermal plasma as a source of highly reactive species, including radicals, photons, atomic and molecular ions, and electrons, which can be transported into the plasma-liquid interface (PLI). The injection of energetic species at the PLI has been used to drive electrochemical reactions, such as carbon dioxide reduction, 10 ammonia synthesis, 11,12 and the hydrogen evolution reaction. 13,14 Reduction—oxidation (redox) chemistry in plasma-liquid systems has also been demonstrated in the context of plasma-activated water, which focuses on the aqueous chemistry induced by reactive oxygen and nitrogen species (RONS). 15,16 However, to date, a comprehensive framework for understanding how to control the reactions occurring on the liquid side of the PLI has not been clearly elucidated, which frustrates efforts to achieve desired chemical transformations. We have recently proposed that the framework of electrochemistry can be used to conceptualize the liquid side of the plasma-liquid system, 17 wherein solid electrodes are now electrodeless near the PLI. However, the spatial locations of the electrodeless cathode and anode within the liquid have not been previously reported, thus the idea itself must be tested, which is the purpose of this work.

Electrochemical reactions are understood in terms of intrinsically coupled reduction and oxidation half-reactions, which describe the overall charge-transfer processes of the redox reaction in the liquid. The basic idea is that reduction

half-reactions are coupled to oxidation half-reactions to preserve both the charge and atom balance in solution. In conventional electrochemical systems, the half-reactions simultaneously occur at interfaces of the working and counter electrodes. In plasma-assisted electrochemistry configurations, which are systems wherein the working electrode is replaced by a DC microplasma, the half-reactions take place at the counter electrode and the PLI.<sup>18</sup> Electrolytic systems capable of initiating redox reactions using reactive species without requiring electrical contact with a counter electrode have been described as a form of electrodeless electrochemical systems. 19-21 One such example of an electrodeless system is a free atmospheric pressure plasma jet (APPJ) impinging upon a liquid solution (Figure 1). The absence of solid electrodes obscures the locations of the half-reactions (i.e. the locations of the electrodeless cathode and anode). Consequently, there is a lack of understanding of where the half-reactions occur in electrodeless plasma-liquid electrochemical systems. We previously developed a framework for electrochemically characterizing a free APPJ in contact with an electrolyte solution.<sup>17</sup> The technique was based on using a reference electrode to measure the local potential within the liquid directly underneath the electrochemically active PLI,  $E_{rz}$ , and

Received: November 8, 2021 Revised: December 24, 2021 Published: January 10, 2022





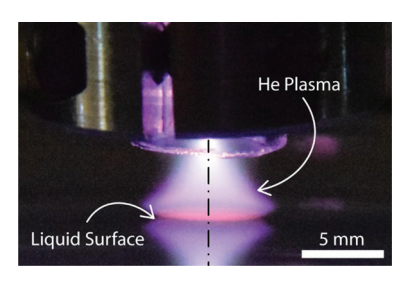


**Figure 1.** Atmospheric pressure plasma jet. Image of helium atmospheric pressure plasma jet (APPJ) in contact with the solution used in this work. Dotted dash line is added to indicate the APPJ centerline.

referencing that measurement to the potential of a nominally identical reference electrode positioned far away in the bulk solution,  $E_{\rm inf}$ . The relative reduction potential measured between the reference electrodes within the solution is given by

$$\eta_{\rm rz} = E_{\rm rz} - E_{\rm inf} \tag{1}$$

A negative potential was observed, suggesting that the reduction-half-reaction (i.e., electrodeless cathode) was taking place directly underneath the PLI. Thus, the complementary

oxidation half-reaction (i.e., electrodeless anode) is expected to be occurring elsewhere in solution.

In this work, we investigate the spatial electrochemical behavior of aqueous solutions exposed to a nonthermal radiofrequency (RF) helium APPJ to elucidate the locations of the redox half-reactions. Electrochemical characterization was based on a previously developed technique, 17 which was adapted to perform measurements as a function of radial distance from the APPJ centerline and depth below the PLI. Based on the signs of the potentials measured by the spatial electrochemical profiles, two distinct regions were observed: a negative region directly underneath the PLI and a positive region in the immediately surrounding solution. In situ multispectral imaging experiments were conducted using colorimetric probe molecules to independently determine where the electrochemical half-reactions were taking place. Visualization of the spatial distribution of redox products was achieved using white light illumination in conjunction with a scientific camera equipped with a bandpass filter. Reduction of the molecular indicator was only detected underneath the APPJ centerline, while the formation of oxidation products was found to occur at larger lateral distances. A surprising finding of our work, which has not previously been discussed in the existing plasma-liquid literature, is that the plasma-liquid

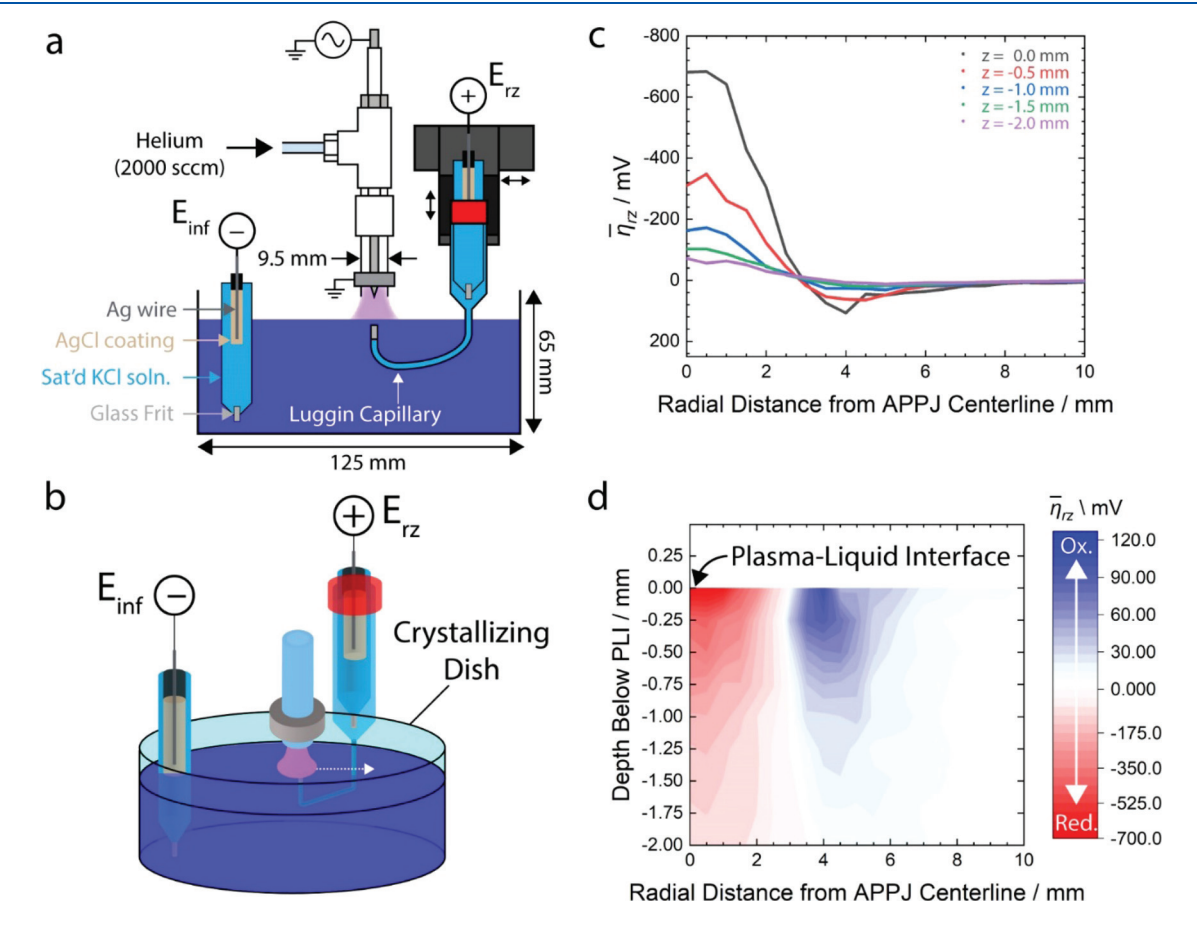


Figure 2. Spatial reduction potential distribution near the plasma—liquid interface (PLI). (a) Schematic representation of plasma jet and scanning reference electrode,  $E_{r,v}$  housed in a Luggin capillary used to measure the local potential in the liquid near the plasma—liquid interface with respect to an identical reference electrode fixed in the bulk solution,  $E_{inf}$ . (b) Schematic illustrating the experimental apparatus used to measure the relative reduction potential profiles near the atmospheric pressure plasma jet (APPJ) centerline showing axial symmetry. (c) Examples of time-averaged relative reduction potential profiles,  $\overline{\eta}_{rv}$ , as a function of radial distance, r, from the APPJ centerline at various depths, z, below the PLI. (d) Contour map generated from the data in (c). Negative potentials (red) are regions where reduction is favored, and positive potentials (blue) are regions where oxidation is favored.

interface simultaneously acts as both the cathode and anode, which occur in spatially distinct locations within the solution.

## METHODS

**Materials.** Indigo carmine (IC, 85%) and titanium(IV) oxysulfate (TiOSO<sub>4</sub>) solution (1.9–2.1%) were purchased from MilliporeSigma. Sodium hydroxide (NaOH, 85%) was purchased from Fisher Scientific. Hydrogen peroxide ( $\rm H_2O_2$ , 35 wt %) was purchased from Acros Organics. All chemicals were used as received without further purification. All solutions were prepared using Type III ultrapure (18.2 MΩ cm) water from a Direct-Q 3 Water Purification System (MilliporeSigma).

**Plasma System.** The plasma source used in this work was an APPJ generated using helium (He) as the operating gas, as shown in Figure 1. The He flow rate was maintained at a constant value of 2000 standard cubic centimeters per minute (sccm) using a mass flow controller (GE50A, MKS Instruments). The plasma was generated using a RF power supply (AG 0613, T&C Power Conversion) connected to an impedance matching network (AIT-600 RF Auto Tuner, T&C Power Conversion). An RF setpoint power of 40 W was used in all experiments. The APPI was comprised of a powered nickel needle electrode with an outer diameter of 2.34 mm housed within a fused silica tube with inner and outer diameters of 7 and 9.5 mm, respectively. The ground electrode was an aluminum ring with an inner diameter of 9.5 mm, which was mounted to the exterior of the silica tube 5 mm from the tube outlet. The APPJ was attached to a micrometer positioning stage in order to maintain a gap height of 5 mm between the end of the silica tube and the surface of the solution undergoing treatment.

Spatial Electrochemical Measurements. Spatial electrochemical measurements were performed within the liquid using the experimental apparatus shown in Figure 2a,b, which is an adaptation of the setup reported in our previous work.<sup>17</sup> Here, the reference electrode used to measure the local potential in the solution near the PLI  $(E_{rz})$  was sealed in a Luggin capillary (Adams & Chittenden) which was mounted on a motorized two-axis stage (X-XY-LSM100A, Zaber Technologies) and controlled using LabView (National Instruments). The glass frit at the end of the Luggin capillary had an outer diameter (OD) of 3.0 mm. The reference electrode measuring the potential in the bulk solution  $(E_{inf})$ remained fixed at a position far from the PLI. The reference electrodes were connected to a digital multimeter (DMM6500, Keithley) and the relative potential differences,  $\eta_{rz}$ , were recorded via LabView. Axial symmetry was assumed for the electrochemical measurements, which were conducted in a 740 mL crystallizing dish containing freshly prepared IC solution with a nominal concentration of 25  $\mu$ M. The pH of the IC solution was adjusted to 11 using NaOH and verified using a pH probe (PHE-1478, Omega Engineering). For a fixed depth below the PLI, radial electrochemical measurements were performed by positioning the Luggin capillary directly underneath the centerline of the APPJ and using the motorized stage to move radially outward in 0.5 mm increments. To obtain a depth profile, the radial measurements were acquired at various depths below the PLI in increments of 0.25 mm. The potential difference near the PLI and bulk solution was measured for a duration of 45 s for each radial distance from the APPJ centerline and depth below the PLI. The potential

differences at each position are reported as time-averaged values,  $\overline{\eta}_{rr}$ .

UV-Vis Absorption Spectroscopy. Ultraviolet-visible (UV-Vis) absorption spectroscopy was used to verify the characteristic wavelengths of the molecular probes, which were used as the central wavelengths for the bandpass filters in the in situ multispectral imaging experiments. All UV-Vis absorption spectroscopy was conducted on a Cary 5000 (Varian) using a scan rate of 150 nm/min over the range of 350-700 nm. Solutions containing molecular probes were treated in glass petri dishes with an OD = 50 mm and height (h) of 15 mm. A freshly prepared IC solution with a nominal concentration of 50  $\mu$ M and an adjusted pH of 11 was used to verify the characteristic wavelengths for both the reduction of  $IC^{2-}$  and formation of  $H_2O_2$ . For the reduction of  $IC^{2-}$ , sample volumes of 20 mL were taken from the same 50 µM IC stock solution and plasma-treated for durations of 2, 4, and 6 min. Changes in pH measured before and after treatment were found to decrease only by 0.2 pH units. A separate untreated control (i.e., 0 min plasma treatment) was set aside for comparison. Aliquots of 2 mL were taken from each petri dish immediately after plasma treatment and characterized using UV-Vis absorption spectroscopy. The titanium sulfate method was used to monitor the formation of H2O2 via the complex that forms between titanium sulfate, which has a strong absorbance centered around 408 nm. 22 Sample volumes of 20 mL from the same 50  $\mu$ M IC stock solution were plasmatreated for 2, 4, 6, 8, and 10 min. To verify the observed change in absorbance at 408 nm was due to H<sub>2</sub>O<sub>2</sub> formation rather than interference from reduced H<sub>2</sub>IC<sup>2-</sup>, differences in the 408 nm absorbance between plasma-treated IC solutions with and without the addition of TiOSO<sub>4</sub> were compared. Two aliquots were drawn for a given treatment time: 200 µL of TiOSO<sub>4</sub> was added to the first aliquot to quantify the amount of  $H_2O_2$  formed, while 200  $\mu L$  of ultrapure water was added to the second aliquot to maintain the same dilution factor. Standards with concentrations of 0 and 50  $\mu$ M H<sub>2</sub>O<sub>2</sub> were also prepared using the same 50  $\mu M$  IC stock solution for comparison.

Multispectral Imaging. In situ multispectral imaging was used to visualize the spatial distribution of redox products in solution as a result of plasma treatment. The multispectral imaging experiments were performed using an LED light source as a white light illumination source, which was passed through a rectangular macro-quartz cuvette (102.5  $\times$  12.5  $\times$  45 mm, FireflySci., Inc.). The macro-cuvette was filled with a total volume of 45 mL of solution prior to each experiment and positioned underneath the APPJ centerline. A freshly prepared 50  $\mu$ M IC solution for visualizing both IC<sup>2-</sup> reduction and H<sub>2</sub>O<sub>2</sub> formation. The cuvette was filled with 45 mL of the stock solution for monitoring the reduction of IC2-, while a mixture of 1 mL TiOSO<sub>4</sub> and 44 mL of the stock solution was used to detect the formation of H<sub>2</sub>O<sub>2</sub>. Images were acquired with a CMOS camera (Atlas 5.0 MP Mono, Sony Pregius IMX250 CMOS, LUCID Vision Labs), which was controlled using the ArenaView (LUCID Vision Labs) software package. All images were acquired using a frame rate of 10 frames per second, a pixel format of 16 bits per pixel, and a pixel resolution of 2448  $\times$  2048. The reduction of IC<sup>2-</sup> was imaged using a 600 nm bandpass filter (65-163, Edmund Optics) with a full width-half max (FWHM) of 10 nm with an exposure time of 8000  $\mu$ s. The formation of  $H_2O_2$  was imaged using a 400 nm bandpass filter (65-132, Edmund Optics) with a

FHWM of 10 nm using an exposure time of  $6000 \mu s$ . Additional details regarding the image processing procedure can be found in Supporting Note 1 of the Supporting Information (SI).

## ■ RESULTS AND DISCUSSION

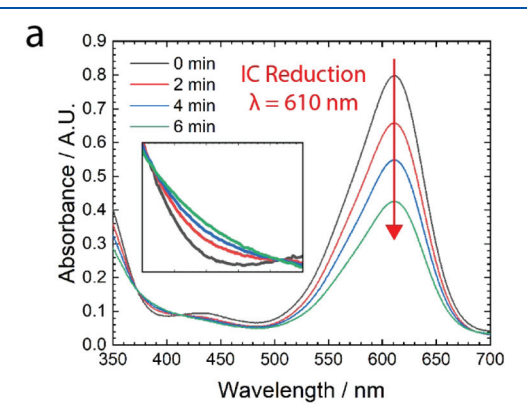
Spatial electrochemical mapping of the time-averaged potential  $(\overline{\eta}_{\rm rz})$  in solution near the active PLI revealed regions with more negative and positive potentials with respect to the bulk solution as shown in Figure 2c,d. The time-averaged values were determined by averaging the  $\eta_{\rm rz}$  values acquired over the 45 s duration at each spatial location using

$$\overline{\eta}_{rz} = \frac{1}{N} \sum_{i=1}^{N} \eta_{rz}(i) \tag{2}$$

where N is the total number of measurements made over the acquisition period and  $\eta_{rz}(i)$  is the relative reduction potential value of the ith measurement. Qualitatively, the radial profiles of  $\overline{\eta}_{rz}$  showed similar trends at each depth below the PLI (Figure 2c). The main influence of varying the depth below the PLI had on the electrochemical measurements was on the observed magnitude of  $\overline{\eta}_{rz}$ . The magnitude of  $\overline{\eta}_{rz}$  was greatest immediately underneath the PLI, suggesting that the electrochemical half-reactions occur at higher rates closer to the surface. As the  $E_{rz}$  reference electrode moved away from the surface, the magnitude of  $\overline{\eta}_{rz}$  decreased with increasing depth, suggesting that the measured potential approaches that of the bulk solution. Given that varying the depth had no observable influence on the sign of  $\overline{\eta}_{rz}$ , the radial distribution of  $\overline{\eta}_{rz}$  was explored to understand where the half-reactions were taking place.

For a fixed depth, the electrochemical profiles revealed that the sign of  $\overline{\eta}_{rz}$  had undergone an inversion as the radial distance from the APPJ centerline was increased, as shown in Figure 2c. A similar measurement technique has been utilized in corrosion research, termed the scanning reference electrode technique (SRET), wherein potential variations between reference electrodes in a solution are used to identify the locations of cathodic and anodic reactions in systems without an external circuit (e.g. a piece of metal corroding in saline water).<sup>23</sup> In the field of corrosion, cathodic and anodic sites on electrochemically active surfaces are identified by regions with potential differences that are more negative and positive, respectively. 23,24 Figure 2c shows that the sign of  $\overline{\eta}_{rz}$  was negative for all  $r \le 2.5$  mm from the APPJ centerline. Following the same convention as the SRET, the negative sign of  $\overline{\eta}_{rz}$  (i.e., more negative value) would suggest that the reduction half-reaction is favored at radial distances closest to the PLI, which is consistent with the observed behavior from our previous work. <sup>17</sup> In fact,  $\overline{\eta}_{rz}$  was found to be most negative at radial distances of  $r \le 0.5$  mm from the APPJ centerline regardless of depth below the PLI. As the radial distance from the APPJ increased, the sign of  $\overline{\eta}_{rz}$  became less negative and experienced an inversion from negative to positive at  $r \approx 3.0$ mm (Figure 2c,d). Positive values of  $\overline{\eta}_{rz}$  indicate that the complementary oxidation half-reaction occurs in this region immediately surrounding the reduction half-reaction. The value of  $\overline{\eta}_{rz}$  became increasingly positive and reached a maximum at a radial distance of  $r \approx 4.0$  mm. Further than 4.0 mm from the jet centerline, the value of  $\overline{\eta}_{rz}$  decreased to approximately zero for  $r \ge 8.0$  mm, meaning the electrochemical activity was indistinguishable from that of the bulk solution.

In addition to spatial electrochemical mapping, spectrophotometric methods were used to identify products of reactions between the plasma and electrolytic solution. The redox indicator IC is commercially available in its oxidized state (IC<sup>2-</sup>) with a characteristic absorption peak at 610 nm (Figure 3a). When IC<sup>2-</sup> is reduced to  $H_2IC^2$ , this characteristic peak



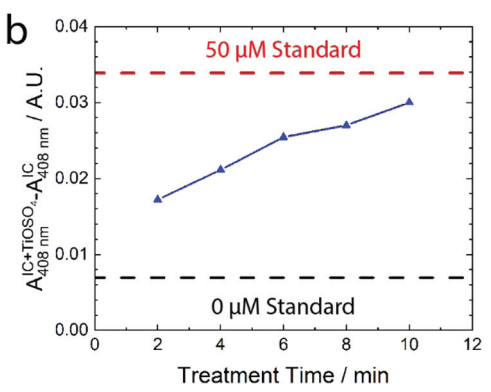


**Figure 3.** UV–Vis absorption spectra of redox products. (a) Absorption spectrum of  $50~\mu\mathrm{M}$  indigo carmine (IC) solutions treated with helium plasma for various treatment times. Red arrow indicates the peak used to observe reduction of IC<sup>2–</sup> in multispectral imaging experiments. Inset illustrating the changing baseline at 408 nm. (b) Change in absorbance at 408 nm of  $50~\mu\mathrm{M}$  IC solutions after plasma treatments for various durations. The plotted value is the difference in absorbance between with and without titanium oxysulfate (TiOSO<sub>4</sub>) in solution. Dashed lines indicate the absorbance at 408 nm of standards with the specified concentration of  $\mathrm{H_2O_2}$  and TiOSO<sub>4</sub>.

decreases, as demonstrated in the UV-Vis absorption spectra of plasma-treated IC solutions shown in Figure 3a. The reduction of IC2- occurs through a two-proton, two-electron transfer process. The change in concentration for IC<sup>2-</sup> after plasma treatment can be determined based on the changes in absorbance at 610 nm. The absorbance peak decreased from 0.798 to 0.425 for treatment times of 0 and 6 min, respectively. Using a calibration curve (SI, Supporting Note 2), the change in absorbance was found to correspond to a reduction of 19.9  $\mu$ M, which would require a stoichiometric equivalence of 39.8  $\mu$ M protons. Given the proton concentration in solution before plasma treatment was on the order of  $10^{-5} \mu M$ , the protons used in the reduction of IC<sup>2-</sup> must have been produced by a reaction promoted by the plasma-liquid interface. A likely proton generating reaction is water oxidation, which produces both protons and hydrogen peroxide. 25-27 Hydrogen peroxide

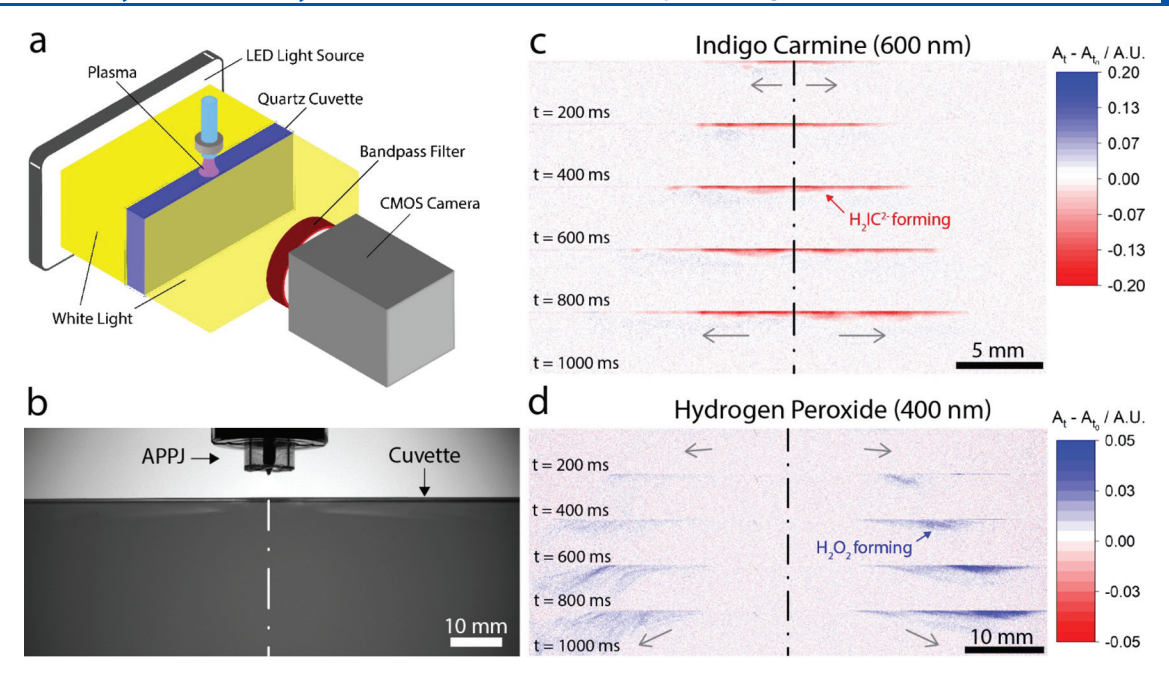


Figure 4. Multispectral imaging. (a) Schematic illustrating the multispectral imaging apparatus to visualize redox reactions in plasma-treated solutions. (b) A representative raw image of a 50  $\mu$ M IC solution undergoing plasma treatment taken with the CMOS camera acquired using an exposure time of 8000  $\mu$ s with a 600 nm bandpass filter. (c) Images of 50  $\mu$ M IC solution acquired with a 600 nm bandpass filter at various times after plasma ignition. (d) Images of 50  $\mu$ M IC solutions with excess TiOSO<sub>4</sub> acquired with a 400 nm bandpass filter at various times after plasma ignition. Dotted-dashed lines indicate the atmospheric pressure plasma jet (APPJ) centerline, and gray arrows indicate the flow direction of the species in the liquid.

(H<sub>2</sub>O<sub>2</sub>) is an oxidant and a long-lived species that is well known to be produced in atmospheric plasma systems that are in contact with an aqueous solution, and in addition to water oxidation, it can also form as a result of recombination of gas phase hydroxyl radicals in the liquid.  $^{14,28}$  Detection of  $\mathrm{H}_2\mathrm{O}_2$ can be achieved using colorimetric methods, such as the titanium sulfate method.<sup>22</sup> The titanium sulfate method involves the formation of a complex between H2O2 and titanium sulfate that has a deep yellow color with an absorbance at 408 nm; a wavelength at which interference from reduced H<sub>2</sub>IC<sup>2-</sup> is minimized (Figure 3a). Thus, differences in the absorbance between plasma-treated IC solutions with and without the addition of titanium(IV) oxysulfate (TiOSO<sub>4</sub>) were compared to characterize the formation of H<sub>2</sub>O<sub>2</sub> (Figure 3b). Using these molecular probes and their characteristic absorption features, in situ multispectral imaging was used to spatially visualize where molecular products of reduction and oxidation formed as a result of plasma treatment.

Multispectral imaging was performed using a CMOS camera equipped with a bandpass filter corresponding to the characteristic wavelength of the species of interest, determined via UV—Vis absorption spectroscopy. Only images acquired at short times after plasma ignition were considered, whereat convolution by transport effects was minimized. The full details of the imaging processing can be found in Supplementary Note 1 in the SI. Briefly, an initial image was acquired prior to igniting the plasma and used as the reference frame. The spatially-resolved pixel intensities for frames acquired after plasma ignition were processed with respect to that reference frame to produce still images of the spatiotemporal changes in absorbance, shown in Figure 4. Thus, negative values (red) correspond to a decreasing

absorbance, while positive values (blue) correspond to an increasing absorbance at a particular position and wavelength.

Multispectral imaging experiments revealed that both H<sub>2</sub>IC<sup>2-</sup> and H<sub>2</sub>O<sub>2</sub> were formed in spatially distinct regions within the solution (Figure 4). Within 10 s of plasma ignition, transport effects were observed to result in mixing and recirculation of products and the bulk solution (SI, Supporting Note 3), thus only short time scales were considered to determine where redox products were forming. The processed multispectral still images in Figure 4 show the changes in absorbance at various times after plasma ignition with respect to an initial frame acquired prior to turning the plasma on. Multispectral imaging of IC using a 600 nm filter revealed that the reduction of IC<sup>2-</sup> was confined near the PLI, aligned directly underneath the APPJ centerline (Figure 4c). Shortly after the plasma was ignited, the reduced product was transported laterally outward. Multispectral imaging of H<sub>2</sub>O<sub>2</sub> was performed by adding TiOSO<sub>4</sub> to an IC solution with a 400 nm bandpass filter. The formation of H<sub>2</sub>O<sub>2</sub> was only observed at lateral distances of approximately 10 mm or greater from the APPJ centerline, as shown in Figure 4d. As time elapsed after igniting the plasma, H<sub>2</sub>O<sub>2</sub> began to move laterally outward. The results are consistent with other reports of plasma-induced chemistry using colorimetric probes, where the reaction emanates from the plasma-liquid interface and transports to the bulk with increasing time.<sup>29</sup> The spatial distributions of both IC and H<sub>2</sub>O<sub>2</sub> were found to be slightly asymmetric about the APPJ centerline, but more pronounced in the case of H<sub>2</sub>O<sub>2</sub>. Relative to the APPJ centerline, H<sub>2</sub>O<sub>2</sub> appears to move downward within the solution on the left-hand side, while accumulating near the surface on the right-hand side (Figure

To account for the dispersion of the products, still images were used to generate lateral profiles of the changes in

absorbance. These profiles were generated by averaging over a depth of 2.0 mm at a given lateral position. The lateral profiles of the change in absorbance at 1 s after plasma ignition are shown in Figure 5 for both IC and  $H_2O_2$ . In the case of IC, the

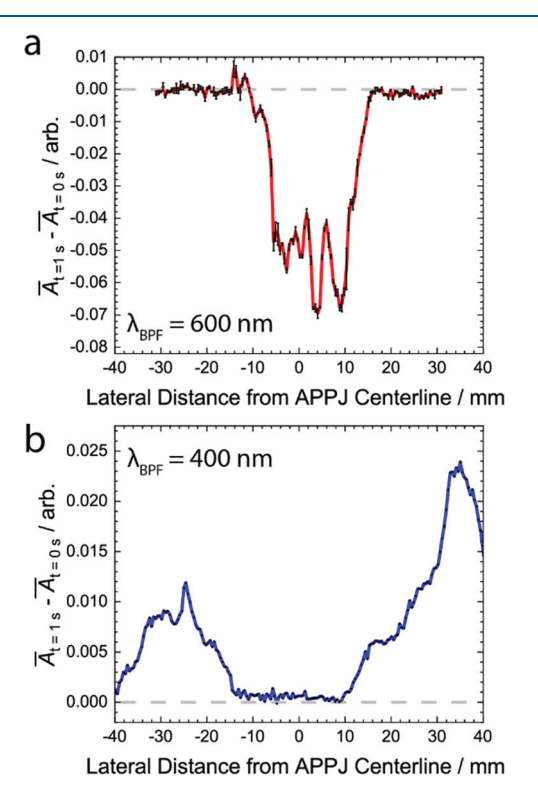


**Figure 5.** Lateral profiles of average absorbance change. (a) Profile of the change in absorbance at 600 nm generated using the multispectral image of  $\rm IC^{2-}$  reduction from Figure 4c, 1 s after plasma ignition. (b) Profile of the change in absorbance at 400 nm generated using the multispectral image of  $\rm H_2O_2$  formation from Figure 4d, 1 s after plasma ignition. Data were binned to increase the signal-to-noise ratio, and black error bars are the standard deviation of absorbance due to shot-to-shot variations on a time scale of 20 ms (images not shown). Dashed gray line is the baseline.

average change in absorbance was found to be negative for lateral distances of approximately  $|x| \le 14$  mm with respect to the APPJ centerline as shown in Figure 5a, which is consistent with the reduction reaction occurring near the plasma jet centerline. For |x| > 14 mm, the average change in absorbance goes to zero, indicating that the IC solution in this region remained unchanged relative to the initial solution. Conversely, the average change in absorbance for H2O2 was found to be zero for lateral distances  $|x| \le 13$  mm, suggesting that  $H_2O_2$ was not forming close to the APPJ centerline as shown in Figure 5b. At greater lateral distances from the APPJ centerline, the average change in absorbance became increasingly positive reaching a maximum at approximately |x| = 30 mm, suggesting that  $H_2O_2$  is most favorably formed in the region surrounding the PLI. Even further away from the jet centerline beyond  $|x| \ge 30$  mm, the value of the average absorbance decreased toward the baseline value of zero. The pH change for the IC solution used in the multispectral imaging experiments was found to be negligible, changing from 11.2 to 11.0 after treatment. Since IC is a pH-dependent redox indicator, multispectral imaging was also performed on a pHindependent indicator (see Supporting Note 4 in SI) to verify

that the observed behavior was due to redox chemistry rather than a possible localized instantaneous pH effect.

While the spatial electrochemical measurements and multispectral imaging experiments revealed the same qualitative trend, namely, reduction reactions occurring near the PLI with the complementary oxidation half-reactions taking place in the surrounding solution, there is a discrepancy in the characteristic lengths between the two methods. More specifically, the boundary between the half-reactions was found to occur at a radial distance of  $r \approx 3.0$  mm in the spatial electrochemical measurements and at a lateral distance of |x| < 13-14 mm for the multispectral imaging experiments. One plausible reason for this discrepancy is the size of the Luggin capillary used to make the measurements near the PLI. While the radial measurements were performed in increments of 0.5 mm, the diameter of the probe was 3.0 mm. Thus, the actual distances between the reduction and oxidation zones may be distorted. A key difference between the two data sets was the vessel geometry and size used in the experiments for each method (Figures 2b and 4a), which would likely influence the transport and recirculation of species between the two characterization techniques. For multispectral imaging experiments, solutions were plasma-treated in a rectangular quartz cuvette with dimensions of  $102.5 \times 12.5 \times 45 \text{ mm}$   $(l \times w \times h)$ . Unfortunately, the reference electrodes used for electrochemical measurements had outer diameters of 16 mm, and thus, the spatial electrochemical characterization could not be performed simultaneously in the vessel used for imaging. Instead, electrochemical characterization was performed in cylindrical vessels with a diameter of 125 mm and a height of 65 mm (Figure 2a). Furthermore, transport effects (Figure 4) likely broaden the data in Figure 5 when compared to Figure 2.

# CONCLUSIONS

In summary, a helium RF plasma jet impinging on an aqueous solution containing the redox indicator IC was used as a model system to identify where redox half-reactions occur in electrodeless plasma-liquid configurations. The conclusions of this work are supported by two independent experimental methods of in situ electrochemical measurements and multispectral imaging using colorimetric molecular indicators. Reduction reactions take place near the plasma jet centerline, and oxidation reactions take place in the adjacent solution. Spatial electrochemical measurements revealed values of  $\bar{\eta}_{rz}$ that were negative for 0 < r < 2.5 mm, and positive for  $3.0 \le r$ < 8.0 mm; indicative of reduction and oxidation half-reactions, respectively. The multispectral imaging results revealed a decreased absorbance for IC at 600 nm for  $|x| \le 14$  mm, suggesting that IC<sup>2-</sup> was reduced to H<sub>2</sub>IC<sup>2-</sup> in that region. The addition of TiOSO<sub>4</sub> to the IC solution showed an increased absorbance at 400 nm for  $|x| \ge 13$  mm, indicative of the formation of a product of water oxidation H<sub>2</sub>O<sub>2</sub>. The results of both data sets suggest that the electrodeless cathode is located directly underneath the PLI, while the electrodeless anode is surrounding in the adjacent solution. Despite the apparent disparity in the characteristic lengths of electrodeless anode and cathode between the two experimental methods, the data sets show the same qualitative behavior. More specifically, the electrodeless cathode is located directly underneath the PLI, while the electrodeless anode is in the surrounding solution.

#### ASSOCIATED CONTENT

# **Supporting Information**

The Supporting Information is available free of charge at https://pubs.acs.org/doi/10.1021/acs.jpcc.1c09650.

Detailed explanation of the multispectral imaging processing procedure, indigo carmine calibration curve, a discussion of transport effects and supplementary multispectral imaging experiments using a pH-independent redox couple (PDF)

## AUTHOR INFORMATION

#### **Corresponding Author**

Elijah Thimsen — Department of Energy, Environmental and Chemical Engineering and Institute of Materials Science and Engineering, Washington University, Saint Louis, Missouri 63130, United States; orcid.org/0000-0002-7619-0926; Email: elijah.thimsen@wustl.edu

#### **Author**

Trey Oldham — Department of Energy, Environmental and Chemical Engineering, Washington University, Saint Louis, Missouri 63130, United States; orcid.org/0000-0002-4058-1490

Complete contact information is available at: https://pubs.acs.org/10.1021/acs.jpcc.1c09650

#### **Author Contributions**

The manuscript was written through contributions of all authors.

#### Notes

The authors declare no competing financial interest.

#### ACKNOWLEDGMENTS

This work was financially supported by the U.S. Department of Energy under award number DE-SC0020352 and the National Science Foundation under grant CBET 2033714.

## ABBREVIATIONS

APPJ, atmospheric pressure plasma jet; IC, indigo carmine; PLI, plasma-liquid interface; RF, radiofrequency; sccm, standard cubic centimeters per minute; UV-Vis, ultraviolet-visible

#### REFERENCES

- (1) Weiss, M.; Barz, J.; Ackermann, M.; Utz, R.; Ghoul, A.; Weltmann, K.-D.; Stope, M. B.; Wallwiener, D.; Schenke-Layland, K.; Oehr, C.; et al. Dose-Dependent Tissue-Level Characterization of a Medical Atmospheric Pressure Argon Plasma Jet. ACS Appl. Mater. Interfaces 2019, 11, 19841–19853.
- (2) Wenzel, T.; Carvajal Berrio, D. A.; Daum, R.; Reisenauer, C.; Weltmann, K.-D.; Wallwiener, D.; Brucker, S. Y.; Schenke-Layland, K.; Brauchle, E.-M.; Weiss, M. Molecular Effects and Tissue Penetration Depth of Physical Plasma in Human Mucosa Analyzed by Contact- and Marker-Independent Raman Microspectroscopy. ACS Appl. Mater. Interfaces 2019, 11, 42885–42895.
- (3) Labay, C.; Roldán, M.; Tampieri, F.; Stancampiano, A.; Bocanegra, P. E.; Ginebra, M.-P.; Canal, C. Enhanced Generation of Reactive Species by Cold Plasma in Gelatin Solutions for Selective Cancer Cell Death. ACS Appl. Mater. Interfaces 2020, 12, 47256–47269.
- (4) Bratescu, M. A.; Cho, S.-P.; Takai, O.; Saito, N. Size-Controlled Gold Nanoparticles Synthesized in Solution Plasma. *J. Phys. Chem. C* **2011**, *115*, 24569–24576.

- (5) Maguire, P.; Rutherford, D.; Macias-Montero, M.; Mahony, C.; Kelsey, C.; Tweedie, M.; Pérez-Martin, F.; McQuaid, H.; Diver, D.; Mariotti, D. Continuous In-Flight Synthesis for On-Demand Delivery of Ligand-Free Colloidal Gold Nanoparticles. *Nano Lett.* **2017**, *17*, 1336–1343.
- (6) Borude, R. R.; Sugiura, H.; Ishikawa, K.; Tsutsumi, T.; Kondo, H.; Ikarashi, N.; Hori, M. Single-Step, Low-Temperature Simultaneous Formations and in Situ Binding of Tin Oxide Nanoparticles to Graphene Nanosheets by In-Liquid Plasma for Potential Applications in Gas Sensing and Lithium-Ion Batteries. ACS Appl. Nano Mater. 2019, 2, 649–654.
- (7) Locke, B. R.; Sato, M.; Sunka, P.; Hoffmann, M. R.; Chang, J.-S. Electrohydraulic Discharge and Nonthermal Plasma for Water Treatment. *Ind. Eng. Chem. Res.* **2006**, *45*, 882–905.
- (8) Stratton, G. R.; Dai, F.; Bellona, C. L.; Holsen, T. M.; Dickenson, E. R. V.; Mededovic Thagard, S. Plasma-Based Water Treatment: Efficient Transformation of Perfluoroalkyl Substances in Prepared Solutions and Contaminated Groundwater. *Environ. Sci. Technol.* 2017, 51, 1643–1648.
- (9) Singh, R. K.; Fernando, S.; Baygi, S. F.; Multari, N.; Thagard, S. M.; Holsen, T. M. Breakdown Products from Perfluorinated Alkyl Substances (PFAS) Degradation in a Plasma-Based Water Treatment Process. *Environ. Sci. Technol.* **2019**, *53*, 2731–2738.
- (10) Mota-Lima, A. The Electrified Plasma/Liquid Interface as a Platform for Highly Efficient CO2 Electroreduction to Oxalate. *J. Phys. Chem. C* **2020**, *124*, 10907–10915.
- (11) Sakakura, T.; Murakami, N.; Takatsuji, Y.; Haruyama, T. Nitrogen Fixation in a Plasma/Liquid Interfacial Reaction and Its Switching between Reduction and Oxidation. *J. Phys. Chem. C* **2020**, 124, 9401–9408.
- (12) Toth, J. R.; Abuyazid, N. H.; Lacks, D. J.; Renner, J. N.; Sankaran, R. M. A Plasma-Water Droplet Reactor for Process-Intensified, Continuous Nitrogen Fixation at Atmospheric Pressure. *ACS Sustainable Chem. Eng.* **2020**, *8*, 14845–14854.
- (13) Mizuno, T.; Akimoto, T.; Azumi, K.; Ohmori, T.; Aoki, Y.; Takahashi, A. Hydrogen Evolution by Plasma Electrolysis in Aqueous Solution. *Jpn. J. Appl. Phys.* **2005**, *44*, 396.
- (14) Mota-Lima, A.; do Nascimento, J. F.; Chiavone-Filho, O.; Nascimento, C. A. O. Electrosynthesis via Plasma Electrochemistry: Generalist Dynamical Model To Explain Hydrogen Production Induced by a Discharge over Water. *J. Phys. Chem. C* **2019**, *123*, 21896–21912.
- (15) Rezaei, F.; Vanraes, P.; Nikiforov, A.; Morent, R.; De Geyter, N. Applications of Plasma-Liquid Systems: A Review. *Materials* **2019**, 12, 2751.
- (16) Zhou, R.; Zhou, R.; Wang, P.; Xian, Y.; Mai-Prochnow, A.; Lu, X.; Cullen, P. J.; Ostrikov, K.; Bazaka, K. Plasma-Activated Water: Generation, Origin of Reactive Species and Biological Applications. *J. Phys. D: Appl. Phys.* **2020**, *53*, 303001.
- (17) Oldham, T.; Chen, M.; Sharkey, S.; Parker, K. M.; Thimsen, E. Electrochemical Characterization of the Plasma-Water Interface. *J. Phys. D: Appl. Phys.* **2020**, *53*, 165202.
- (18) Witzke, M.; Rumbach, P.; Go, D. B.; Sankaran, R. M. Evidence for the Electrolysis of Water by Atmospheric-Pressure Plasmas Formed at the Surface of Aqueous Solutions. *J. Phys. D: Appl. Phys.* **2012**, *45*, No. 442001.
- (19) Bardwell, J. A.; Foulds, I. G.; Webb, J. B.; Tang, H.; Fraser, J.; Moisa, S.; Rolfe, S. J. A Simple Wet Etch for GaN. *J. Electron. Mater.* 1999, 28, L24–L26.
- (20) Hwang, Z. H.; Hwang, J. M.; Hwang, H. L.; Hung, W. H. Electrodeless Wet Etching of GaN Assisted with Chopped Ultraviolet Light. *Appl. Phys. Lett.* **2004**, *84*, 3759–3761.
- (21) Green, R. T.; Tan, W. S.; Houston, P. A.; Wang, T.; Parbrook, P. J. Investigations on Electrode-Less Wet Etching of GaN Using Continuous Ultraviolet Illumination. *J. Electron. Mater.* **2007**, *36*, 397–402.
- (22) Eisenberg, G. Colorimetric Determination of Hydrogen Peroxide. *Ind. Eng. Chem., Anal. Ed.* 1943, *15*, 327–328.

- (23) Isaacs, H.; Vyas, B. Scanning Reference Electrode Techniques in Localized Corrosion. In Electrochemical Corrosion Testing; Mansfeld, F., Bertocci, U., Eds.; ASTM International: 100 Barr Harbor Drive, PO Box C700, West Conshohocken, PA, 1981; pp 3-31.
- (24) Voruganti, V. S.; Luft, H. B.; DeGeer, D.; Bradford, S. A. Scanning Reference Electrode Technique for the Investigation of Preferential Corrosion of Weldments in Offshore Applications. Corrosion 1991, 47, 343-351.
- (25) McDonnell-Worth, C.; Mac Farlane, D. R. Ion Effects in Water Oxidation to Hydrogen Peroxide. RSC Adv. 2014, 4, 30551-30557.
- (26) Siahrostami, S.; Li, G.-L.; Viswanathan, V.; Nørskov, J. K. Oneor Two-Electron Water Oxidation, Hydroxyl Radical, or H<sub>2</sub>O<sub>2</sub> Evolution. J. Phys. Chem. Lett. 2017, 8, 1157-1160.
- (27) Shi, X.; Siahrostami, S.; Li, G.-L.; Zhang, Y.; Chakthranont, P.; Studt, F.; Jaramillo, T. F.; Zheng, X.; Nørskov, J. K. Understanding Activity Trends in Electrochemical Water Oxidation to Form Hydrogen Peroxide. Nat. Commun. 2017, 8, 701.
- (28) Naitali, M.; Kamgang-Youbi, G.; Herry, J.-M.; Bellon-Fontaine, M.-N.; Brisset, J.-L. Combined Effects of Long-Living Chemical Species during Microbial Inactivation Using Atmospheric Plasma-Treated Water. Appl. Environ. Microbiol. 2010, 76, 7662-7664.
- (29) Volkov, A. G.; Bookal, A.; Hairston, J. S.; Roberts, J.; Taengwa, G.; Patel, D. Mechanisms of Multielectron Reactions at the Plasma/ Water Interface: Interfacial Catalysis, RONS, Nitrogen Fixation, and Plasma Activated Water. Electrochim. Acta 2021, 385, No. 138441.



## **Atomic-Scale Etching Mechanism of Aluminum with** Fluorine-Based Plasma

Abu Asaduzzaman.

AUGUST 12, 2022

THE JOURNAL OF PHYSICAL CHEMISTRY C

READ **Z** 

**High-Performance Photoelectrochemical Enzymatic** Bioanalysis Based on a 3D Porous Cu<sub>2</sub>O@TiO, Film with a Solid-Liquid-Air Triphase Interface

Hongli Cheng, Xinjian Feng, et al.

DECEMBER 05, 2022

LANGMUIR

READ 🗹

# **Local Electric Field and Electrical Conductivity Analysis** Using a Glass Microelectrode

Tatsunori Kishimoto and Kentaro Doi

OCTOBER 21, 2022

ACS OMEGA

READ **'** 

# Effects of Relative Humidity and Paper Geometry on the **Imbibition Dynamics and Reactions in Lateral Flow Assays**

Debayan Das, Aashish Priye, et al.

AUGUST 01, 2022

LANGMUIR

READ 🗹

Get More Suggestions >